Unraveling the Molecular Mechanisms of ABHD5 Membrane Targeting

Short Title: ABHD5 Membrane binding

Amit Kumar[a], Matthew Sanders[b], Huamei Zhang[b], Li Zhou[b], Shahnaz Parveen[a], Christopher V. Kelly[a], James G. Granneman[b,c], and Yu-ming M. Huang[a]*

[a]Department of Physics and Astronomy, Wayne State University, Detroit, MI 48201, USA

[b]Center for Molecular Medicine and Genetics, School of Medicine, Wayne State University, Detroit, MI 48201, United States

[c]Center for Integrative Metabolic and Endocrine Research, School of Medicine, Wayne State University, Detroit, MI 48201, United States

*corresponding author:

Yu-ming M. Huang

E-mail: ymhuang@wayne.edu

Phone: 1-313-577-3280

ORCID: 0000-0003-3257-6170

Abstract

ABHD5 plays a critical role in lipid metabolism, regulating fatty acid mobilization, skin barrier formation, and phospholipid remodeling. ABHD5 lacks catalytic activity and instead functions as an essential co-regulator of PNPLA enzymes. Understanding how ABHD5 interacts with lipid droplet (LD) and endoplasmic reticulum (ER) membranes is crucial for unraveling its regulatory role in lipid metabolism and identifying potential therapeutic targets for metabolic diseases. While previous studies have modeled ABHD5 structure in solution, its function relies on membrane interactions, requiring a detailed investigation of its binding mechanisms. In this study, we employed multiscale simulations with experimental validation to reveal how ABHD5 interacts with ER and LD. Our findings show that ABHD5 binds membranes through its N-terminus and insertion segment, which subsequently triggers structural changes in the pseudosubstrate pocket and alters lipid distribution. This study also identifies key residues essential for membrane binding, providing potential targets for developing lipid metabolism modulators. These results uncover a previously unrecognized mechanism by which ABHD5 interacts with membranes, offering new insights into lipolysis regulation and potential therapeutic strategies for metabolic diseases.

Key words: α/β-hydrolase domain-containing protein, lipid homeostasis, protein-membrane interaction, molecular dynamics, metabolic regulation

Significance

Lipid droplets (LDs) are central to cellular energy regulation, yet the structural mechanisms by which proteins bind and remodel LD membranes have remained poorly understood. This study provides the first molecular-level insights into how proteins interact with LDs and drive membrane remodeling. By integrating multiscale simulations with experimental validation, we reveal that ABHD5 binds to LD surfaces by adopting an open-pocket conformation, which enables it to exploit packing defects created by neutral lipids. This unique structural adaptation allows ABHD5 to interact with and reshape LD membranes effectively. Our findings establish a mechanistic framework for understanding protein-mediated LD dynamics, highlighting the critical role of neutral lipids in facilitating protein binding and membrane remodeling.

Introduction

The importance of lipid metabolism in cell function and systemic health is profound, as lipids serve as key components of cellular membranes, signaling molecules, and energy reserves (1–4). Dysregulation of lipid metabolism is linked to various diseases, including obesity, diabetes, cardiovascular disorders, and skin barrier dysfunction, highlighting the need to understand how lipid homeostasis is maintained in different cell types and tissues (5–8).

α/β-hydrolase domain-containing protein 5 (ABHD5) is emerging as a critical regulator of diverse lipid metabolic pathways, including fatty acid mobilization from adipocytes and muscle (9, 10), skin barrier formation by keratinocytes (11, 12), and phospholipid remodeling in hepatocytes (13). The molecular mechanisms by which ABHD5 controls these diverse pathways are poorly understood. Although most pathways regulated by ABHD5 involve triacylglycerol (TAG) hydrolysis, ABHD5 is a pseudoenzyme without inherent catalytic activity (14, 15). Instead, it functions as an essential regulator of specific members of the patatin-like phospholipase domain-containing (PNPLA) family (16–18). For example, in keratinocytes, ABHD5 inactivation prevents the activation of PNPLA1, disrupting the formation of acyl-ceramides in the endoplasmic reticulum (ER) that is necessary for the skin barrier (19, 20). In the heart, ABHD5 deficiency leads to severe TAG accumulation and premature death in mice, likely due to the loss of PNPLA2 function on lipid droplets (LD) (21). These examples illustrate how ABHD5 enables PNPLA family members to access substrates localized to LD and ER membranes.

The proper binding and orientation of ABHD5 to ER and LD membranes is crucial for the activation of PNPLA enzymes, yet the structural basis of membrane targeting is incompletely understood. Despite the lack of an experimental structure for ABHD5, elucidating these mechanisms could provide valuable insights into the regulation of lipid pathways and identify

potential therapeutic targets for metabolic diseases. Previous efforts were confined to NMR analysis of its disordered N-terminus (39 residues) (22), revealing multiple unstructured peptides in solution but failing to determine a membrane structure or provide insights into its ligand-binding pocket, protein-protein interaction surfaces, or membrane-binding sites. Later, homology and deep learning methods were employed to model ABHD5 structure in solution (23). The machine learning model (24) was found to be the most consistent with experimentally validated protein-protein interaction surfaces and ligand binding sites. The modeled structure of ABHD5 demonstrated a canonical hydrolase fold, comprising six α helices, eight β sheets, and two flexible regions (23). These flexible regions encompass the N-terminus (residues 1-43), which is known to interact with the membrane through key tryptophan residues (W21, W25, and W29), and the insertion segment of residues 180-270, forming a pseudosubstrate pocket that can bind endogenous and synthetic ligands, promoting or repressing ABHD5 activation (25, 26). However, all prior studies rely on ABHD5 structures modeled in solution. The absence of an ABHD5-membrane complex structure hinders a comprehensive understanding of its role in lipolysis and lipid metabolism, given that all these processes occur on or involve membrane interactions.

Modeling protein conformation on membranes is challenging, as current tools like PPM Web Server (27) and DREAMM (28) focus on transmembrane proteins and peripheral proteins interacting with bilayers, which do not accommodate ABHD5 due to its disordered N-terminus and the unique LD monolayer. Traditional all-atom (AA) and coarse-grained (CG) molecular dynamics (MD) simulations have been combined to overcome these limitations, as seen in studies like the insertion of Ca^{2+}-independent phospholipase A2 (iPLA2) into a bilayer (29). This study investigates the interactions of ABHD5 with ER and LD membranes by constructing bilayer and trilayer systems, respectively, using CGMD for diffusion studies and Gaussian accelerated MD

(GaMD) for detailed conformational analysis. We aim to identify specific residues involved in membrane binding and study changes in the ABHD5 pseudosubstrate pocket, providing insights into interactions with proteins like PNPLA2 in lipolysis and identifying potential therapeutic targets for lipid metabolic diseases.

Results

ABHD5 must be targeted/trafficked to LDs to regulate lipolysis, yet its orientation to the membrane surface is unknown. We conducted diffusion simulations to investigate ABHD5-membrane interactions. Modeling this diffusion process using AA models for the entire ABHD5 protein (containing 351 residues) with the membrane is highly time-consuming. Therefore, we applied CGMD simulations to observe the process by which the ABHD5 protein binds to the membrane. We then refined the resulting complex structure into AA models to study the detailed interactions between ABHD5 and the membrane. Subsequently, we identified residues in contact with the membrane and compared our results with mutagenesis experiments (**Figure 1**).

Dual-site membrane binding mechanism of ABHD5

To explore the structural basis of ABHD5-membrane binding, we first performed full protein diffusion simulations using CGMD. These simulations identified two main regions where ABHD5 interacts with the membrane: the N-terminal 43 amino acids and the part of the insertion segment forming the pseudosubstrate pocket between amino acids 180 and 230 (**Figure 2**). We found that the N-terminal amino acids serve as the initial anchor interacting with the membrane. Both our ER and LD simulations demonstrated that the N-terminal region interacts with the membrane around 1 μs. Three tryptophans (W21, W25, and W29) in the N-terminus stably associate with the membrane, aligning well with findings from a previous study (22). Then, the second contact site, the pseudosubstrate pocket begins interacting with the membrane around 1.2-

1.4 μs (**Movie 1 and 2**). This site, identified through our CGMD simulations, has not been previously implicated in membrane targeting.

To quantify the lipid components involved in protein-membrane binding, we calculated the contact time between each ABHD5 residue and lipids from ER and LD (**Figure 2A and 2B**). Our analysis of ABHD5-ER interaction occupancy revealed that POPC forms strong interactions (i.e., >40% of simulation time) with residues W21, W25, W29, W199, and Y272, and moderate interactions (10-40% of time) with residues A202, A205, A206, W210, F222, and W274. DOPE and SAPI primarily exhibit moderate or weak (<10% of time) interactions with the same set of residues (**Figure 2A, S1A, S1B, and S2A**). In the ABHD5-LD system, POPC strongly interacts with residues W21, W25, and W29, and moderately interacts with residues W181, W199, F210, F222, Y272, Y274, C301, and H329. DOPE and SAPI also show moderate interactions with the same group of residues, except for W181, C301, and H329 (**Figure 2B, S1C, S1D, and S2B**).

Atomistic insights into ABHD5-membrane interactions

We refined the ABHD5-ER and ABHD5-LD complex structures from CG to AA models and conducted GaMD simulations to examine the detailed interactions between ABHD5 and the membrane. Atomistic interactions, such as hydrogen bonding, are not captured by the CG model but were analyzed using AAMD. **Figures 3A and S3A** show the equilibrated structures of ABHD5 binding to both the ER and LD. In the refined AAMD simulations, we found that the overall structure, such as the key membrane-binding amino acids from ABHD5, remained the same. However, the flexible N-terminal and the insertion segment exhibited slightly different equilibrium conformations.

In the N-terminus, aromatic residues such as tryptophan (W21, W25, and W29) and hydroxyl-containing threonine residues (T23 and T28) play a crucial role in protein-membrane

interactions (**Figure 3B and S3B**). These residues can adopt conformations that allow them to form hydrogen bonds with the phospholipid headgroups, while their hydrophobic sidechains embed into the nonpolar core formed by phospholipid tails or TAG. The N-terminal segment, residues 22-26, is particularly important, as it consistently penetrated the membrane in all MD simulation replicas. Moreover, part of the pseudosubstrate pocket diffuses into the membrane, with residues 198-207 forming a lid helix (**Figure 3C and S3C**)). This helix is primarily composed of hydrophobic residues (V198, W199, I200, A202, V203, G204, A205, A206, L207), whose hydrophobic sidechains interact with the lipid tails or TAG, while the polar mainchain and R201 sidechain interact with lipid headgroups. The insertion segment also includes additional hydrophobic residues (209–230). The aromatic rings of these hydrophobic residues play a critical role in membrane targeting by facilitating interactions with neighboring residues and lipids through π-stacking. Notably, W199, F210, and F222 form a hydrophobic patch essential for LD association. Both the ER and LD use the same binding mode for membrane interactions.

To evaluate how deeply ABHD5 penetrates the ER and LD membranes, we computed the distance between each residue and the membrane surface (**Figure 3D**). Our results show that ~40 residues of ABHD5 (out of a total of 351) are buried within the membrane for both ER and LD binding. ABHD5 interacts with both membranes at similar depths, with the average distance of each residue from the membrane surface being around 15 Å. However, the specific regions of ABHD5 that come closer to the membrane differ between the ER and LD. For example, residues 285-325 are positioned closer to the membrane in LD compared to their positioning in the ER. The average distance between residues 285-325 and the membrane is 22.0 ± 4.2 Å for the ER and 13.0 ± 7.0 Å for the LD. Notably, this region (285-325) is significant as it may act as the interface for interactions with other protein partners, such as PNPLA or PLIN (30, 31). Moreover, after MD

equilibration, we found fewer hydrogen bonds between ABHD5 and the LD membrane (**Figure 3E**). This reduction is due to TAG molecules in the LD penetrating the phospholipid-rich upper leaflet and forming hydrophobic interactions with ABHD5, particularly in the insertion segment, thus decreasing hydrogen bonding after equilibration.

Experimental validation of ABHD5 hydrophobic patch in LD targeting

Both CGMD and AAMD reveal that key interaction motifs, including central residues W199, F210, and Y222, as well as N-terminal residues W21, W25, and W29, directly interact with TAG near the LD surface (**Figure 2B**), facilitating LD targeting. To experimentally test the significance of these motifs, we mutated these residues to alanine and examined their targeting to LD in transfected Cos7 cells and to artificial lipid droplets (aLD). Wild-type (WT) ABHD5 tagged with cyan fluorescent protein (CFP) was co-transfected with W199A-F210A-F222A-ABHD5–mCherry and imaged using confocal fluorescence microscopy (**Figure 4A-D**). WT ABHD5 highly targeted to intracellular LD of Cos7 cells as evidenced by strong colocalization with the LD marker Bodipy C-16. In contrast, W199A, F210A, F222 ABHD5-mCherry was nearly completely cytosolic and negligibly associated with LDs. Similarly, W21A-W25A-W29A-ABHD5-YFP displayed significantly weaker LD targeting than WT ABHD5 (**Figure S4**). The proper expression and folding of the mutant ABHD5 was confirmed in separate experiments by co-transfecting it with PLIN5 (aa360-417)-YFP and observing the recovery of the mutant ABHD5 LD association through its intact protein-protein binding interface (**Figure S5**).

To measure the importance of these key residues on the binding rate and equilibrium binding density of ABHD5, we observed their association with aLDs. Cell lysates expressing WT ABHD5, W199A-ABHD5, W181A-ABHD5, or W199A-F210A-F222A-ABHD5 were exposed to aLDs and imaged with confocal fluorescence microscopy (**Figure 4E-G**). While controlling for

the concentration of the surrounding ABHD5, all three mutant ABHD5 bound the aLDs at <25% density as the WT in equilibrium with the triple mutant demonstrating the weakest equilibrium binding equal at 6% of the WT. Whereas W181A-ABHD5 and W199A-F210A-F22A-ABHD5 demonstrated 24% of the aLD binding rate as WT ABHD5, W199A-ABHD5 bound the aLDs at 73% of the initial biding rate as WT. This demonstrates the collective and nuanced contributions of these hydrophobic residues to the mechanism of ABHD5 targeting LDs, including that the central hydrophobic residues contribute more so to the equilibrium LD binding density of ABHD5 than the initial binding LD rate.

ABHD5 structural changes upon membrane binding

RMSF was calculated to assess the conformational flexibility of ABHD5 in solution and when bound to ER and LD membranes (**Figure S6**). Regions with high RMSF values indicate greater flexibility, while low values correspond to more restricted movements during the MD simulation. The RMSF analysis of free and membrane-bound ABHD5 reveals that the N-terminal region and residues 188–210 within the insertion segment exhibit greater flexibility compared to the core region (residues 80–179). The RMSF values for the N-terminal, core region, and residue 188-210 are approximately 1.96, 0.71, and 1.39 Å, respectively. The core region remains generally stable, attributed to intraprotein interactions (**Figure S6**). Notably, residues 250–351 exhibit greater flexibility when bound to the ER membrane than to the LD membrane, as this region is positioned farther from the ER membrane surface and lacks membrane interactions (**Figure 3D**).

Structural analysis of ABHD5 in its free and membrane-bound states reveals that the insertion segment undergoes significant conformational changes upon membrane binding, which regulates the opening and closing of the pseudosubstrate pocket. This process is primarily controlled by the hydrophobic lid helix (residues 198–207). In solution, the lid helix moves toward

the protein core, stabilizing a closed conformation, where hydrophobic residues interact to exclude water (**Figure 5A**). Upon binding to ER (**Figure 5B**) and LD (**Figure 5C**) membranes, the helix shifts away from the core, leading to an open conformation of the pocket. To quantify this transition, the distance between the ABHD5 core region and the lid helix (**Figure 5D**) was measured. Upon membrane binding, this distance increases from 21.8 Å to 33.3 Å for ER and to 32.9 Å for LD, indicating a substantial opening of the pocket required for membrane targeting. These findings highlight the lid helix as a key structural element that regulates the conformational dynamics of the pocket and facilitates ABHD5 interaction with membranes.

Lipid rearrangement and nanodomain formation

The presence of TAG in LD changes how lipids interact with both the N-terminal region and the insertion segment of ABHD5. TAG forms moderate interactions with residues W199, A202, A206, F210, and F222, and weak interactions with residues W21, W25, W29, A205, Y272, and Y274 (**Figure 2B and S2D**), which influences the interaction between ABHD5 and phospholipids. In general, TAG reduces the contact time between POPC and key residues, such as W21, W25, W29, W199, A202, A205, A206, and F222. For example, across three simulation replicas, POPC contact with W199 drops from 56.7% in the ER to 31.6% in the LD (**Table S1**). Conversely, in some instances, TAG increases POPC interactions, such as with W181, where contact rises from 4.8% in the ER to 13.8% in the LD (**Table S1**). However, TAG has little effect on DOPE and SAPI contact times, except for W199, where DOPE contact decreases from 24.2% in the ER to 14.7% in the LD.

We also investigated the spatial distribution of lipids around ABHD5 on both ER and LD membranes (**Figure 6A and 6B**). Our results show that, in both membrane systems, ABHD5 modulates lipid distribution around its pseudosubstrate pocket. In the ER system, POPC clusters

around the pseudosubstrate pocket of ABHD5, while DOPE and SAPI surround the protein (**Figure 6A**). A different lipid distribution is observed in the LD system, where TAG and SAPI accumulate around the pseudosubstrate pocket, excluding POPC and DOPE (**Figure 6B**). The CGMD simulations reveal that ABHD5 remodels the membrane by repelling POPC and DOPE while concentrating SAPI and TAG beneath the protein on the LD surface.

Membrane surface remodeling in LD induced by ABHD5 binding

To assess how ABHD5 binding remodels the membrane surface, we calculated the membrane surface shape from the center of mass positions of phospholipids. The phospholipids were binned across the XY-plane, and the mean phospholipid height in each bin over the last 200 ns of the AAMD simulation was used to calculate the average membrane shape for the ER and LD membranes with and without ABHD5 bound (**Figure 7A and 7B**). Under ABHD5, the average LD phospholipids were elevated 14 ± 5 Å above the surrounding phospholipids. The LD phospholipid elevation extended with a full width at half maximum (FWHM) of 33 ± 3 Å; however, this curvature width may have been artificially reduced due to the finite size of the simulation. The ER membrane shape was minimally affected by ABHD5 binding.

Additionally, changes to the TAG shape were analyzed upon ABHD5 binding to the LD membrane (**Figure 7C and 7D**). The center of mass of each TAG molecule was binned in the XY plane, and the center of mass of the top TAG molecule in each XY bin determined the TAG surface height. Under ABHD5, a TAG nanodomain was formed, with the TAG surface elevated 17 ± 5 Å above the TAG surface far from ABHD5. The TAG nanodomain was more elevated and concentrated under ABHD5 than the change to the phospholipid monolayer (**Figure S7 and Movie 3 and 4**). Changes in membrane shape and the TAG surface over time are shown in **Figure S8-S11**.

Discussion

ABHD5 plays a crucial role in lipid metabolism, with its functional activities occurring exclusively on membranes, including ER and LDs (19–21). While the solution structure of ABHD5 has been previously modeled (23), such structural insights alone are insufficient to elucidate the molecular mechanisms underlying its membrane-associated functions. The study of protein-membrane interactions, especially in systems as complex as ABHD5 and LDs, poses significant challenges. These include the large-scale nature of the system, the intrinsic complexity of LD-associated membranes, and the time-intensive computational demands of simulating diffusion and membrane remodeling processes. In this study, we employed a multiscale simulation framework to investigate ABHD5's binding to ER and LDs, its structural changes, and lipid reorientation within the membrane. CGMD simulations captured large-scale protein diffusion and binding events, while accelerated AAMD simulations provided atomic-level details of ABHD5's interactions with membranes. Our ABHD5-membrane model showed strong agreement with experimental validation, supporting its accuracy in capturing key molecular details. This approach revealed, for the first time, how a protein binds to LDs and alters membrane dynamics. The methodology used here offers a versatile framework for studying protein-membrane interactions in complex biological systems.

The insertion segment of ABHD5 is highly flexible in solution. Our findings reveal that, despite being previously overlooked, this segment plays a critical role in membrane targeting. It can adopt multiple conformations to facilitate membrane interaction. The hydrophobic residues of the insertion segment penetrate the membrane, interacting directly with phospholipid tails or TAGs, while the hydrophilic residues form polar interactions with phospholipid headgroups. This binding mechanism resembles that of certain membrane proteins that utilize amphipathic helices to

associate with lipid bilayers. Amphipathic helices are well-known for recognizing hydrophobic membrane defects, which often arise from bilayer bending (32, 33). For instance, the iPLA2 enzyme (29), which shares an α/β hydrolase domain with ABHD5, stabilizes its interaction with bilayer membranes via an amphipathic helix. Similarly, Protein Kinase C (PKC) uses its C1 domain, containing an amphipathic helix, to bind membranes in response to diacylglycerol (DAG) and phosphatidylserine (PS), anchoring PKC and activating its kinase function (34). Recent studies on Plin4 protein further highlight the role of amphipathic helices in lipid interactions, showing that increased hydrophobic residue size enhances binding to both LDs and bilayers (35). The insertion segment of ABHD5 is enriched with hydrophobic residues, including the lid helix that contains five residues with large non-polar side chains (e.g., valine and tryptophan). This structural feature enables ABHD5 to bind both LD and ER membranes, similar to proteins like Arf, which utilize short helices to interact with both LDs and bilayer membranes (36).

The ABHD5 pseudosubstrate pocket undergoes significant conformational changes upon membrane binding, with the lid helix playing a key role in regulating its opening and closing. A similar structural transition has been observed in lipoprotein-associated phospholipase A2 (Lp-PLA2), where membrane binding expands the pocket, facilitating efficient substrate extraction and binding (37). For ABHD5, our simulations revealed a 1.5-fold increase in the distance between the protein core region and the lid helix (**Figure 5D**), suggesting the flexibility for the pocket (**Figure S6**). To further validate these findings, we used the membrane-bound structure of ABHD5 in its open conformation, manually removed the membrane, and performed GaMD simulations in solution. Our results show that the pseudosubstrate pocket, now exposed to water, gradually transitioned to a closed conformation, with the lid helix shifting toward the protein core region

after 200 ns of simulation time (**Figure S12**). These findings reveal membrane binding stabilizes the open conformation of the pseudosubstrate pocket, while its absence favors a closed state.

Membrane remodeling is typically driven by the interplay of neutral and charged lipids and their interactions with proteins, resulting packing defects or curvature changes that regulate membrane dynamics. The membrane remodeling in ER has been extensively studied (38–40). For example, proteins like α-synuclein create curvature by inserting amphipathic helices (41), while ubiquitin-like proteins modify lipid headgroups, enhancing curvature during autophagy or endocytosis. However, LD membranes exhibit unique properties, such as larger packing defects compared to bilayer or ER membranes, which influence protein interactions and lipid metabolism (42). Neutral lipids, e.g., TAGs, in LDs reduce surface tension and create persistent packing defects to recruit amphipathic helices from Class II LD proteins, such as Perilipins and CCTα, enabling them direct binding to the LD surface from the cytosol (43–45). In this study, we observed ABHD5 binding to LD membrane defects induced by TAG insertion, with TAGs moving into the ABHD5 pseudosubstrate pocket and phospholipid redistribution driving membrane remodeling. The lid helix of ABHD5 further enhanced structural changes on the LD surface, while minimal remodeling occurred at the ER, underscoring the role of neutral lipids (TAGs) in promoting packing defects.

In conclusion, this study investigates how ABHD5 binds to ER and LD membranes, revealing that the insertion segment of ABHD5 plays a critical role in membrane targeting. This process is facilitated by the lid helix that penetrates the membrane and interacts with phospholipid tails or TAGs. Upon membrane binding, the pseudosubstrate pocket undergoes conformational changes, transitioning from a closed to an open conformation. ABHD5 binding also induces membrane remodeling, particularly in LDs, where TAGs move into the pseudosubstrate pocket, altering lipid distribution and creating packing defects that facilitate protein binding. Since

ABHD5 and proteins in the PNPLA/PLIN family coordinate the regulation of lipolysis, future research includes exploring how ABHD5 interacts with PLIN or PNPLA proteins on the LD surface. Moreover, some compounds are known to influence ABHD5's role in lipid metabolism (15, 23, 30), however, their interactions with ABHD5 remain unclear. Modeling ABHD5-compound complexes on LDs assists in designing modulators of lipolysis. This study also highlights membrane remodeling following protein binding; however, the impact of membrane composition, such as changes in phosphatidylethanolamine (PE) levels, which is known to promote membrane curvature in bilayers, needs further investigation in LD systems.

Materials and Methods

A detailed description of the computational and experimental methods is provided in SI Materials and Methods. Briefly, the ABHD5 protein structure was obtained from a previous study, where it was modeled using homology modeling and deep learning tools with experimental validation (23). The ER and LD membrane systems were constructed using CHARMM-GUI (46–49) and PACKMOL (50). CG and AA MD simulations were performed using GROMACS 2020.5 (51) and Amber20 (52–54), respectively, with the MARTINI 3.0 (55), Amber ff14SB (56), Lipid14 (57), and GAFF force fields (58). GaMD simulations were conducted to enhance sampling efficiency. System equilibration and production simulations followed standard protocols, with parameters detailed in **Tables S2** and **S3**. Experimental validation included fluorescence spectroscopy and lipid-binding assays, performed as described in SI Materials and Methods. Trajectory analyses, including RMSF, hydrogen bonding, and lipid distribution, were conducted using VMD (59), PyMOL (60), and CPPTRAJ (61).

Data, Materials, and Software Availability

The simulation input files, resulting trajectories, and post-MD analysis scripts are freely available at https://doi.org/10.5281/zenodo.15122721. All other data are included in the manuscript and/or supporting information.

Acknowledgments

We thank Wayne State University High Performance Computing Center for the support of CGMD and GaMD simulations. This work was supported by the WSU startup grant to Y.M.H., the WSU postdoctoral fellows grant to C.V.K., J.G.G., and Y.M.H., and the NIH grants (R01DK076629 to J.G.G. and C.V.K. and R01DK105963 to J. G. G.).

Author Contributions

A.K. and Y.M.H. designed the project. A.K. performed all simulations. A.K., C.V.K, and Y.M.H. analyzed data. M.S., H.Z., L.Z., S.P., C.V.K, and J.G.G performed experimental work. A.K., C.V.K, J.G.G., and Y.M.H wrote the manuscript.

Competing interests

The authors declare no competing interest.

References

1. H. Sunshine, M. L. Iruela-Arispe, Membrane lipids and cell signaling. *Curr. Opin. Lipidol.* **28**, 408–413 (2017).

2. K. Liu, M. J. Czaja, Regulation of lipid stores and metabolism by lipophagy. *Cell Death Differ.* **20**, 3–11 (2013).

3. F. Khan, *et al.*, Unraveling the intricate relationship between lipid metabolism and oncogenic signaling pathways. *Front. Cell Dev. Biol.* **12**, 1399065 (2024).

4. A. L. Santos, G. Preta, Lipids in the cell: organisation regulates function. *Cell. Mol. Life Sci.* **75**, 1909–1927 (2018).

5. C. Y. Park, *et al.*, Dysregulation of lipid droplet protein expression in adipose tissues and association with metabolic risk factors in adult females with obesity and type 2 diabetes. *J. Nutr.* **153**, 691–702 (2023).

6. Y.-L. Wu, *et al.*, Epigenetic regulation in metabolic diseases: mechanisms and advances in clinical study. *Signal Transduct. Target. Ther.* **8**, 98 (2023).

7. Z. Wang, *et al.*, Metabolic disorders and risk of cardiovascular diseases: A two-sample mendelian randomization study. *BMC Cardiovasc. Disord.* **23**, 529 (2023).

8. A. Srebrnik, S. Brenner, B. Ilie, G. Messer, Dorfman-Chanarin syndrome: Morphologic studies and presentation of new cases. *Am. J. Dermatopathol.* **20**, 79–85 (1998).

9. M. Schweiger, A. Lass, R. Zimmermann, T. O. Eichmann, R. Zechner, Neutral lipid storage disease: genetic disorders caused by mutations in adipose triglyceride lipase/ *PNPLA2* or *CGI-58* / *ABHD5*. *Am. J. Physiol.-Endocrinol. Metab.* **297**, E289–E296 (2009).

10. Y. Son, *et al.*, Adipocyte-specific Beclin1 deletion impairs lipolysis and mitochondrial integrity in adipose tissue. *Mol. Metab.* **39**, 101005 (2020).

11. Y. Ohno, A. Nara, S. Nakamichi, A. Kihara, Molecular mechanism of the ichthyosis pathology of Chanarin–Dorfman syndrome: Stimulation of PNPLA1-catalyzed ω-O-acylceramide production by ABHD5. *J. Dermatol. Sci.* **92**, 245–253 (2018).

12. T. Hirabayashi, *et al.*, PNPLA1 has a crucial role in skin barrier function by directing acylceramide biosynthesis. *Nat. Commun.* **8**, 14609 (2017).

13. G. Teskey, *et al.*, Lipid droplet targeting of the lipase coactivator ABHD5 and the fatty liver disease-causing variant PNPLA3 I148M is required to promote liver steatosis. *J. Biol. Chem.* **301**, 108186 (2025).

14. A. Lass, *et al.*, Adipose triglyceride lipase-mediated lipolysis of cellular fat stores is activated by CGI-58 and defective in Chanarin-Dorfman Syndrome. *Cell Metab.* **3**, 309–319 (2006).

15. M. A. Sanders, H. Zhang, L. Mladenovic, Y. Y. Tseng, J. G. Granneman, Molecular basis of ABHD5 lipolysis activation. *Sci. Rep.* **7**, 42589 (2017).

16. Y. Ohno, A. Nara, S. Nakamichi, A. Kihara, Molecular mechanism of the ichthyosis pathology of Chanarin–Dorfman syndrome: Stimulation of PNPLA1-catalyzed ω-O-acylceramide production by ABHD5. *J. Dermatol. Sci.* **92**, 245–253 (2018).

17. A. Lass, R. Zimmermann, M. Oberer, R. Zechner, Lipolysis – A highly regulated multi-enzyme complex mediates the catabolism of cellular fat stores. *Prog. Lipid Res.* **50**, 14–27 (2011).

18. S. Romeo, D. B. Savage, Lipase tug of war: PNPLA3 sequesters ABHD5 from ATGL. *Nat. Metab.* **1**, 505–506 (2019).

19. T. Nohara, Y. Ohno, A. Kihara, Impaired production of skin barrier lipid acylceramides and abnormal localization of PNPLA1 due to ichthyosis-causing mutations in PNPLA1. *J. Dermatol. Sci.* **107**, 89–94 (2022).

20. B. Kien, *et al.*, ABHD5 stimulates PNPLA1-mediated ω-O-acylceramide biosynthesis essential for a functional skin permeability barrier. *J. Lipid Res.* **59**, 2360–2367 (2018).

21. Z. H. Jebessa, *et al.*, The lipid-droplet-associated protein ABHD5 protects the heart through proteolysis of HDAC4. *Nat. Metab.* **1**, 1157–1167 (2019).

22. A. Boeszoermenyi, *et al.*, Structure of a CGI-58 motif provides the molecular basis of lipid droplet anchoring. *J. Biol. Chem.* **290**, 26361–26372 (2015).

23. R. Shahoei, *et al.*, Molecular modeling of ABHD5 structure and ligand recognition. *Front. Mol. Biosci.* **9**, 935375 (2022).

24. J. Jumper, *et al.*, Highly accurate protein structure prediction with AlphaFold. *Nature* **596**, 583–589 (2021).

25. M. A. Sanders, *et al.*, Endogenous and synthetic ABHD5 ligands regulate ABHD5-Perilipin interactions and lipolysis in fat and muscle. *Cell Metab.* **22**, 851–860 (2015).

26. M. A. Sanders, H. Zhang, L. Mladenovic, Y. Y. Tseng, J. G. Granneman, Molecular basis of ABHD5 lipolysis activation. *Sci. Rep.* **7**, 42589 (2017).

27. M. A. Lomize, I. D. Pogozheva, H. Joo, H. I. Mosberg, A. L. Lomize, OPM database and PPM web server: Resources for positioning of proteins in membranes. *Nucleic Acids Res.* **40**, D370–D376 (2012).

28. A. Chatzigoulas, Z. Cournia, DREAMM: a web-based server for drugging protein-membrane interfaces as a novel workflow for targeted drug design. *Bioinformatics* **38**, 5449–5451 (2022).

29. D. Bucher, Y.-H. Hsu, V. D. Mouchlis, E. A. Dennis, J. A. McCammon, Insertion of the Ca2+-Independent Phospholipase A2 into a phospholipid bilayer via coarse-grained and atomistic molecular dynamics simulations. *PLoS Comput. Biol.* **9**, e1003156 (2013).

30. Y. Y. Tseng, *et al.*, Structural and functional insights into ABHD5, a ligand-regulated lipase co-activator. *Sci. Rep.* **12**, 2565 (2022).

31. J. G. Granneman, H.-P. H. Moore, R. Krishnamoorthy, M. Rathod, Perilipin controls lipolysis by regulating the interactions of AB-hydrolase containing 5 (ABHD5) and adipose triglyceride lipase (ATGL). *J. Biol. Chem.* **284**, 34538–34544 (2009).

32. H. Cui, E. Lyman, G. A. Voth, Mechanism of membrane curvature sensing by amphipathic helix containing proteins. *Biophys. J.* **100**, 1271–1279 (2011).

33. S. Vanni, H. Hirose, H. Barelli, B. Antonny, R. Gautier, A sub-nanometre view of how membrane curvature and composition modulate lipid packing and protein recruitment. *Nat. Commun.* **5**, 4916 (2014).

34. S. S. Katti, *et al.*, Structural anatomy of protein kinase C C1 domain interactions with diacylglycerol and other agonists. *Nat. Commun.* **13**, 2695 (2022).

35. A. Čopič, *et al.*, A giant amphipathic helix from a perilipin that is adapted for coating lipid droplets. *Nat. Commun.* **9**, 1332 (2018).

36. C. Prévost, *et al.*, Mechanism and determinants of amphipathic helix-containing protein targeting to lipid droplets. *Dev. Cell* **44**, 73-86.e4 (2018).

37. V. D. Mouchlis, *et al.*, Lipoprotein-associated phospholipase A_2 : A paradigm for allosteric regulation by membranes. *Proc. Natl. Acad. Sci.* **119**, e2102953118 (2022).

38. A. Gubas, I. Dikic, ER remodeling via ER-phagy. *Mol. Cell* **82**, 1492–1500 (2022).

39. A.-C. Jacomin, I. Dikic, Membrane remodeling via ubiquitin-mediated pathways. *Cell Chem. Biol.* **31**, 1627–1635 (2024).

40. W. Jang, V. Haucke, ER remodeling via lipid metabolism. *Trends Cell Biol.* **34**, 942–954 (2024).

41. J. Varkey, *et al.*, Membrane curvature induction and tubulation are common features of synucleins and apolipoproteins. *J. Biol. Chem.* **285**, 32486–32493 (2010).

42. C. Prévost, *et al.*, Mechanism and determinants of amphipathic helix-containing protein targeting to lipid droplets. *Dev. Cell* **44**, 73-86.e4 (2018).

43. N. Krahmer, *et al.*, Phosphatidylcholine synthesis for lipid droplet expansion is mediated by localized activation of CTP:Phosphocholine cytidylyltransferase. *Cell Metab.* **14**, 504–515 (2011).

44. N. Kory, R. V. Farese, T. C. Walther, Targeting Fat: Mechanisms of Protein Localization to Lipid Droplets. *Trends Cell Biol.* **26**, 535–546 (2016).

45. M. Majchrzak, *et al.*, Perilipin membrane integration determines lipid droplet heterogeneity in differentiating adipocytes. *Cell Rep.* **43**, 114093 (2024).

46. S. Jo, T. Kim, V. G. Iyer, W. Im, CHARMM-GUI: A web-based graphical user interface for CHARMM. *J. Comput. Chem.* **29**, 1859–1865 (2008).

47. J. Lee, *et al.*, CHARMM-GUI input generator for NAMD, GROMACS, AMBER, OpenMM, and CHARMM/OpenMM simulations using the CHARMM36 additive force field. *J. Chem. Theory Comput.* **12**, 405–413 (2016).

48. Y. Qi, *et al.*, CHARMM-GUI martini maker for coarse-grained simulations with the martini force field. *J. Chem. Theory Comput.* **11**, 4486–4494 (2015).

49. E. L. Wu, *et al.*, CHARMM-GUI membrane builder toward realistic biological membrane simulations. *J. Comput. Chem.* **35**, 1997–2004 (2014).

50. L. Martínez, R. Andrade, E. G. Birgin, J. M. Martínez, PACKMOL: A package for building initial configurations for molecular dynamics simulations. *J. Comput. Chem.* **30**, 2157–2164 (2009).

51. D. Van Der Spoel, *et al.*, GROMACS: Fast, flexible, and free. *J. Comput. Chem.* **26**, 1701–1718 (2005).

52. A. W. Götz, *et al.*, Routine microsecond molecular dynamics simulations with AMBER on GPUs. 1. Generalized born. *J. Chem. Theory Comput.* **8**, 1542–1555 (2012).

53. R. Salomon-Ferrer, A. W. Götz, D. Poole, S. Le Grand, R. C. Walker, Routine microsecond molecular dynamics simulations with AMBER on GPUs. 2. Explicit solvent particle mesh ewald. *J. Chem. Theory Comput.* **9**, 3878–3888 (2013).

54. S. Le Grand, A. W. Götz, R. C. Walker, SPFP: Speed without compromise—A mixed precision model for GPU accelerated molecular dynamics simulations. *Comput. Phys. Commun.* **184**, 374–380 (2013).

55. P. C. T. Souza, *et al.*, Martini 3: a general purpose force field for coarse-grained molecular dynamics. *Nat. Methods* **18**, 382–388 (2021).

56. J. A. Maier, *et al.*, ff14SB: Improving the Accuracy of Protein Side Chain and Backbone Parameters from ff99SB. *J. Chem. Theory Comput.* **11**, 3696–3713 (2015).

57. C. J. Dickson, *et al.*, Lipid14: The amber lipid force field. *J. Chem. Theory Comput.* **10**, 865–879 (2014).

58. J. Wang, R. M. Wolf, J. W. Caldwell, P. A. Kollman, D. A. Case, Development and testing of a general amber force field. *J. Comput. Chem.* **25**, 1157–1174 (2004).

59. W. Humphrey, A. Dalke, K. Schulten, VMD: Visual molecular dynamics. *J. Mol. Graph.* **14**, 33–38 (1996).

60. W. L. DeLano, D. Scientific, S. Carlos, PyMOL: An open-source molecular graphics tool.

61. D. R. Roe, T. E. Cheatham, PTRAJ and CPPTRAJ: Software for processing and analysis of molecular dynamics trajectory data. *J. Chem. Theory Comput.* **9**, 3084–3095 (2013).

Figure Legends

Figure 1: Multiscale simulations combined with experiments identify the protein motifs responsible for membrane binding. Our computational workflow incorporates validating and equilibrating the AlphaFold protein structure (A), converting this structure to a CG model (B), simulating the protein conformation changes and membrane remodeling with CGMD (C), and back-conversion and equilibration of the structures with accelerated AAMD (D). Mutagenesis experiments were applied to validate the key protein motifs (E). The ABHD5 N-terminal (residues 1 to 43) is shown in blue. Protein region (consisting of residues 180 to 230), which diffuses to the membrane surface, is shown in magenta and the remaining part of the ABHD5 protein is shown in green. The TAG is shown in gray, phospholipid POPC, DOPE, and SAPI are shown in cyan, and phosphates in POPC, DOPE, and SAPI are shown by orange spheres. The residues (W21, W25, W29, W181, W199, F210, and F222) involved in mutagenesis study are shown as spheres in (E).

Figure 2: Contact frequency of ABHD5 residues with lipids in ER and LD membranes. The percentage of contact time in CGMD simulations between each ABHD5 residue and different lipid components (POPC, DOPE, SAPI, and TAG) in ER and LD membranes is shown in A and B, respectively. Two key regions where ABHD5 interacts with the membrane are highlighted: the N-terminal 43 amino acids and the insertion segment that forms a pseudosubstrate pocket spanning amino acids 180 to 230. A zoomed view of the interaction pattern in these regions is provided in Figure S2. This occupancy data represents the average of contact time from three independent CGMD simulations, with the corresponding error shown in Figure S3.

Figure 3: AAMD simulation of ABHD5-membrane models. (A) A side view of ABHD5 inserted into the LD membrane from a representative simulation snapshot. A curved line indicates the approximate position of the membrane surface. Two key regions, the N-terminus and insertion

segment, where ABHD5 residues diffuse into membrane are highlighted by blue and magenta, respectively. (B) Detailed interactions of the ABHD5 N-terminus and LD. Positively charged residues are shown in blue, polar residues in green, and non-polar residues in gray, all represented in bond form. (C) Detailed interaction of residues 198-230 within the insertion segment and LD. (D) Distance between ABHD5 residues and the membrane surface. Orange and green arrows indicate two hydrophobic regions: one consisting of residues I270, P271, Y272, and G273, and the other comprising residues C301 and I302. (E) Number of hydrogen bonds between ABHD5 and membranes in 1000 ns AAMD simulations.

Figure 4: Confocal fluorescence imaging of live cells and aLDs validate the importance of hydrophobic residues for ABHD5 binding to membranes. (A) WT ABHD5 was targeted to LD and ER membranes, whereas (B) the triple-mutant W199A, F210A, F222A ABHD5 was not. (C) LDs were visualized by their incorporation of Bodipy. (D) The color merge image shows the membrane and LD-bound WT ABHD5 colocalized with the LDs while the mutant ABHD5 is cytosolic and within the nucleus. (E) 3D reconstruction image of artificial LD caps shows the concentration of the ABHD5 variants (yellow) on the membrane (red). (F) Mutation of W181A or the triple mutant decreased binding rate of ABHD5 during the first 5 mins to the aLD surface. (G) After 24 hours of equilibration, all three mutants demonstrate significantly lower equilibrium binding to the aLD than the WT ABHD5. (A-D) The scale bars represent 20 μm.

Figure 5: Conformational changes in ABHD5 upon membrane binding. A representative snapshot of ABHD5 in solution (A) and when bound to ER (B) and LD (C), with the insertion segment highlighted in magenta. The lid helix formed by residues 198-207 is highlighted in pink. The key residues (F86, W181, Y272, and Y330) in the pseudosubstrate pocket for ligand binding

are shown in orange. The distance between the ABHD5 core and the lid helix over the GaMD simulations is shown in (D).

Figure 6: Lipid remodeling. Lipid distribution around ABHD5 on the ER and LD membranes is shown in A and B, where POPC, DOPE, SAPI, and TAG are represented in red, green, blue, and magenta, respectively.

Figure 7: ABHD5 induced local curvature in the LD membrane. Phospholipids near ABHD5 were elevated relative to the surrounding membrane, as shown in (A) the 200 ns time-averaged height map of the LD surface for one replica with ABHD5 (dashed circle) and (B) the radially averaged phospholipid height from the LD center across three replicas per condition. (A) White pixels represent regions where no phospholipids were present. Additionally, TAG molecules beneath ABHD5 were, on average, positioned higher than in regions without ABHD5. This is illustrated in (C) the 200 ns time-averaged TAG height map for one replica with ABHD5 and (D) the radially averaged TAG height for each condition. In (B) and (D), error bars indicate the standard deviation of lipid heights at each radius over the 200 ns window for each replica.

Movie Legends

Movie 1: Modeling the diffusion of ABHD5 to the ER using CGMD. All color representations are consistent with those in Figure 1.

Movie 2: Modeling the diffusion of ABHD5 to the LD using CGMD. All color representations are consistent with those in Figure 1.

Movie 3: Modeling the dynamics of ABHD5 bound to the ER using all-atom GaMD. All color representations are consistent with those in Figure S7.

Movie 4: Modeling the dynamics of ABHD5 bound to the LD using all-atom GaMD. All color representations are consistent with those in Figure S7.

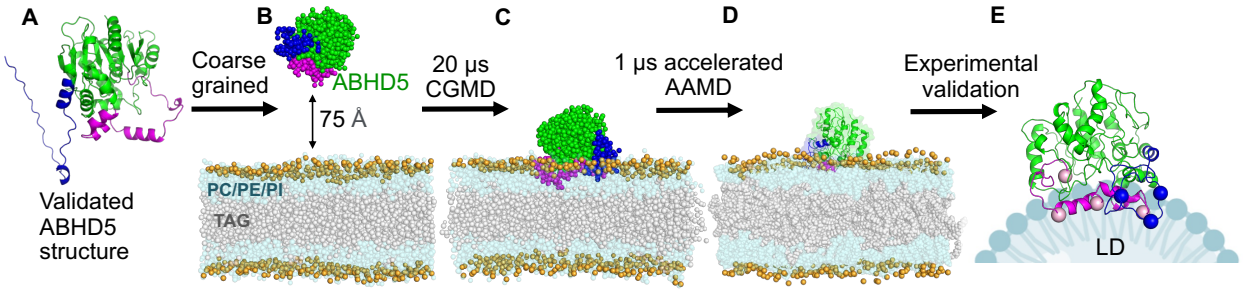
A
B
C
D
E
Coarse grained
ABHD5
75 Å
20 μs CGMD
1 μs accelerated AAMD
Experimental validation
Validated ABHD5 structure
PC/PE/PI
TAG
LD

Figure 1

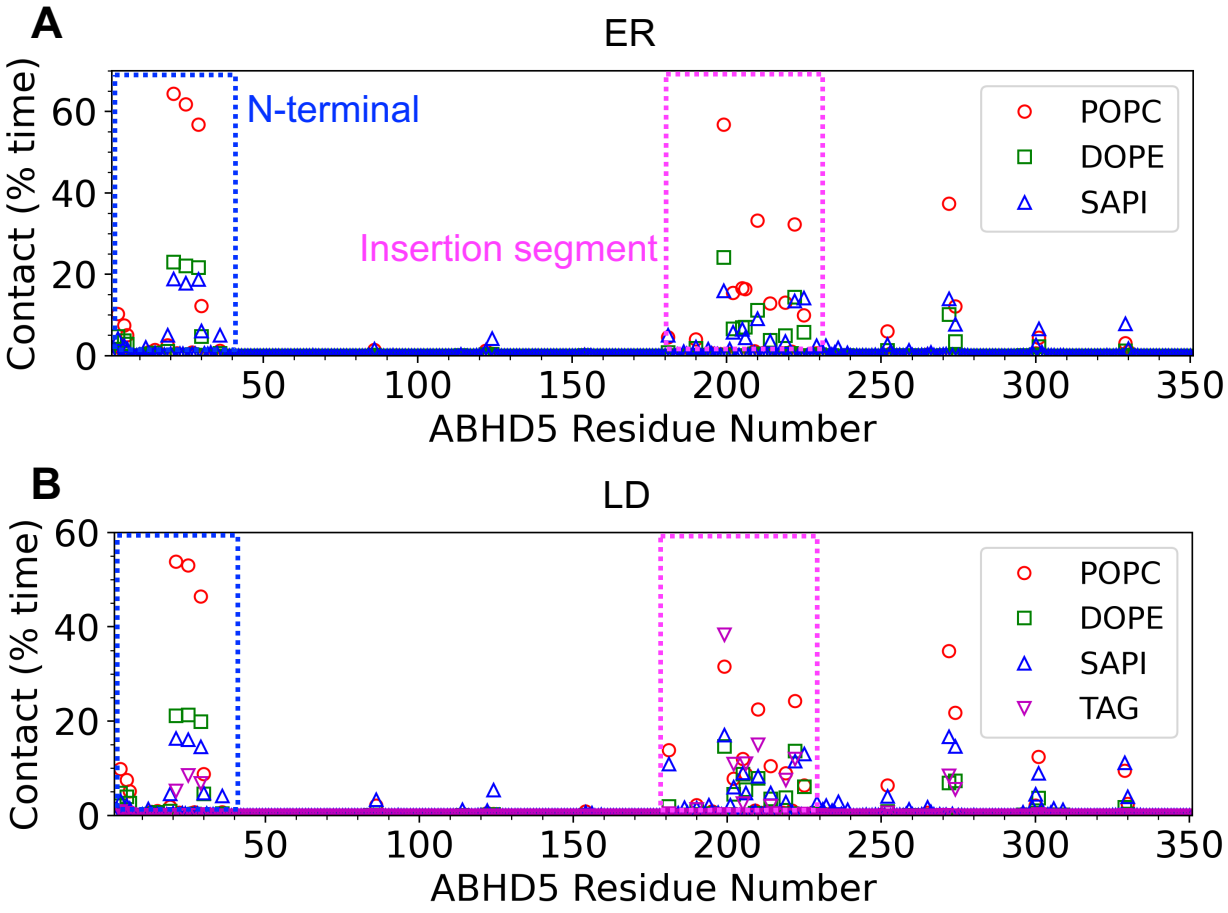
A
ER
N-terminal
Insertion segment
POPC
DOPE
SAPI
Contact (% time)
ABHD5 Residue Number
B
LD
POPC
DOPE
SAPI
TAG
Contact (% time)
ABHD5 Residue Number

Figure 2

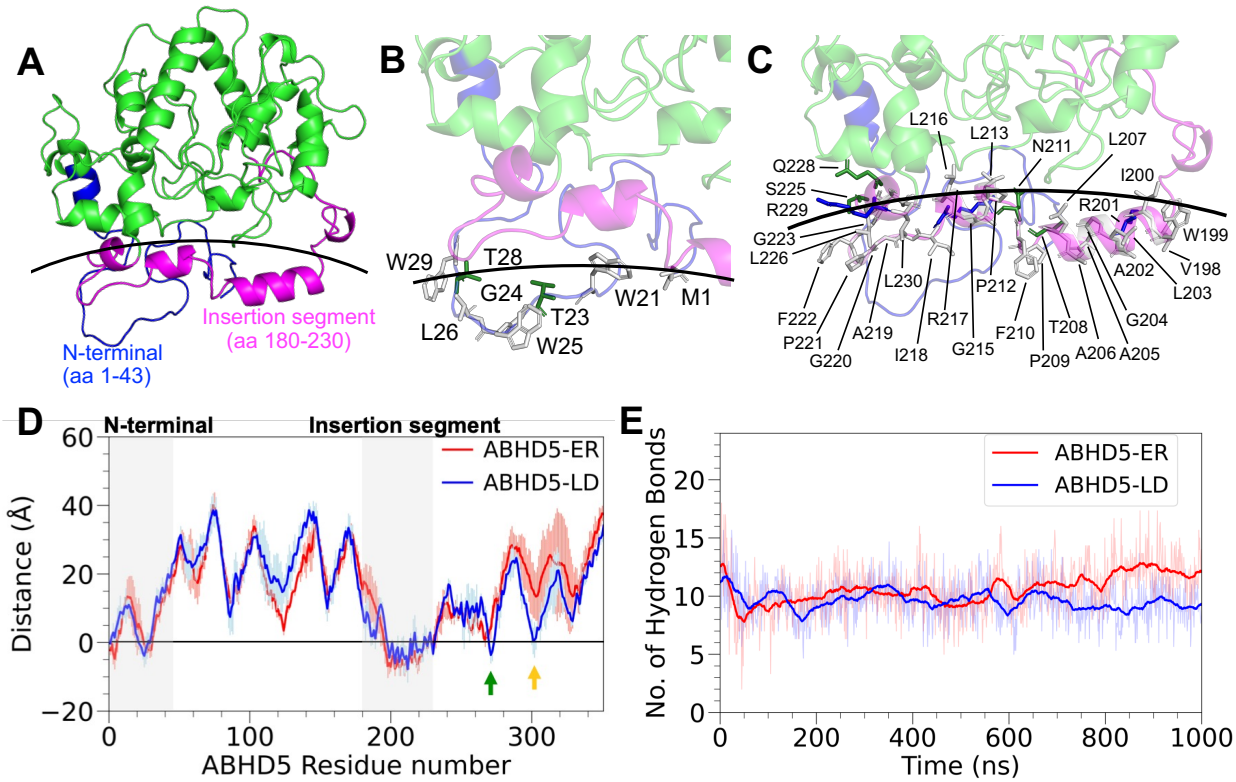
A
N-terminal
(aa 1-43)
Insertion segment
(aa 180-230)
B
W29
T28
G24
T23
W21
M1
L26
W25
C
L216
L213
N211
L207
Q228
I200
S225
R229
R201
G223
W199
L226
A202
V198
L230
P212
L203
F222
R217
G204
A219
F210
T208
P221
I218
G215
A206
A205
G220
P209
D
N-terminal
Insertion segment
ABHD5-ER
ABHD5-LD
Distance (Å)
ABHD5 Residue number
E
ABHD5-ER
ABHD5-LD
No. of Hydrogen Bonds
Time (ns)

Figure 3

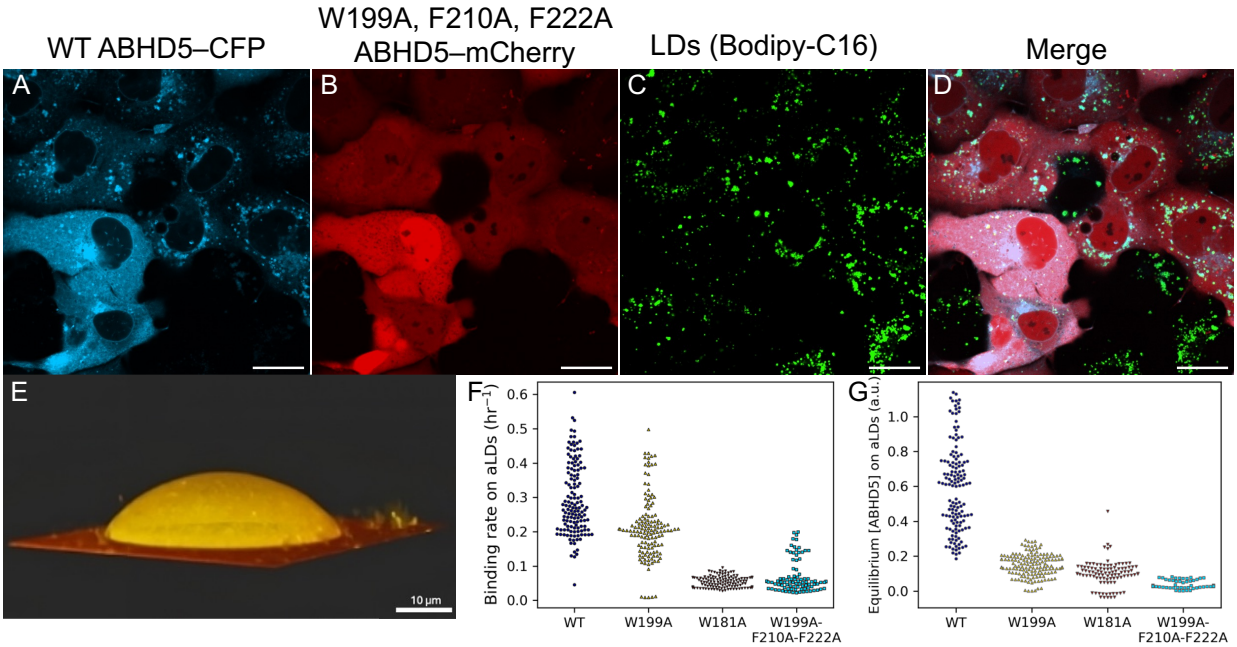
WT ABHD5–CFP
W199A, F210A, F222A ABHD5–mCherry
LDs (Bodipy-C16)
Merge
A
B
C
D
E
10 µm
F
Binding rate on aLDs (hr⁻¹)
0.0
0.1
0.2
0.3
0.4
0.5
0.6
WT
W199A
W181A
W199A-F210A-F222A
G
Equilibrium [ABHD5] on aLDs (a.u.)
0.0
0.2
0.4
0.6
0.8
1.0
WT
W199A
W181A
W199A-F210A-F222A

Figure 4

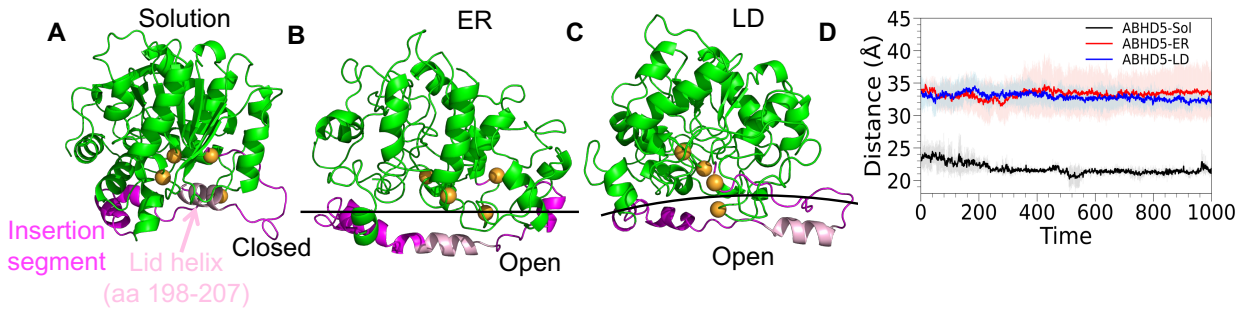
A
Solution
Insertion segment
Lid helix (aa 198-207)
Closed
B
ER
Open
C
LD
Open
D
ABHD5-Sol
ABHD5-ER
ABHD5-LD
Distance (Å)
Time
45
40
35
30
25
20
0
200
400
600
800
1000

Figure 5

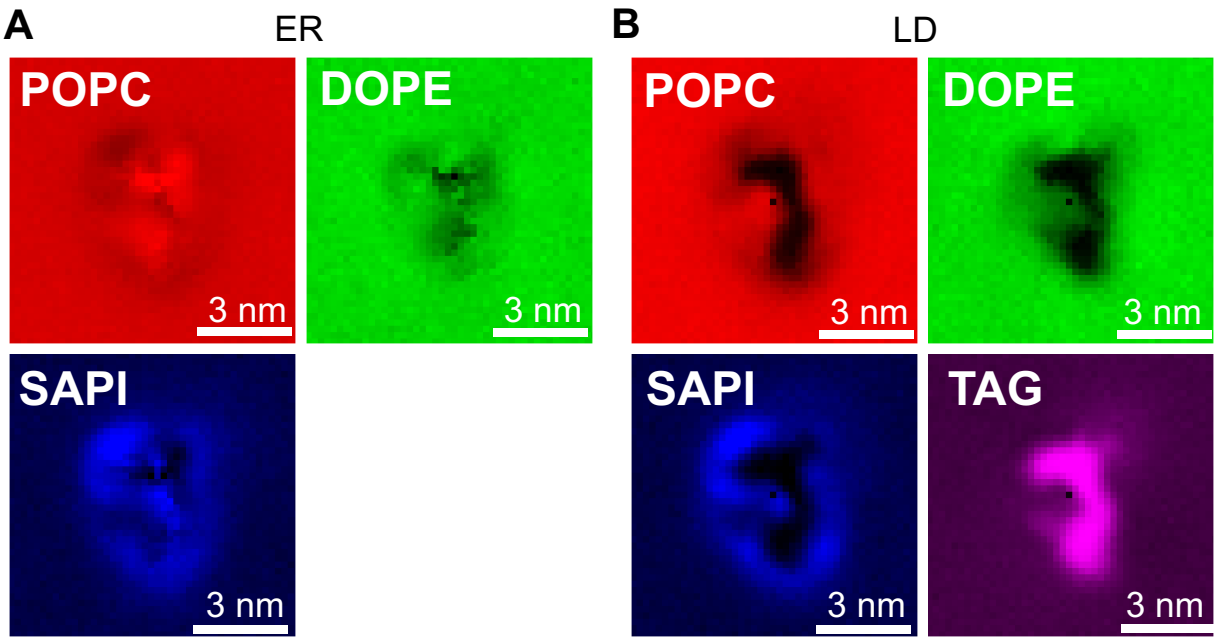
A
ER
POPC
DOPE
SAPI
3 nm
3 nm
3 nm
B
LD
POPC
DOPE
SAPI
TAG
3 nm
3 nm
3 nm
3 nm

Figure 6

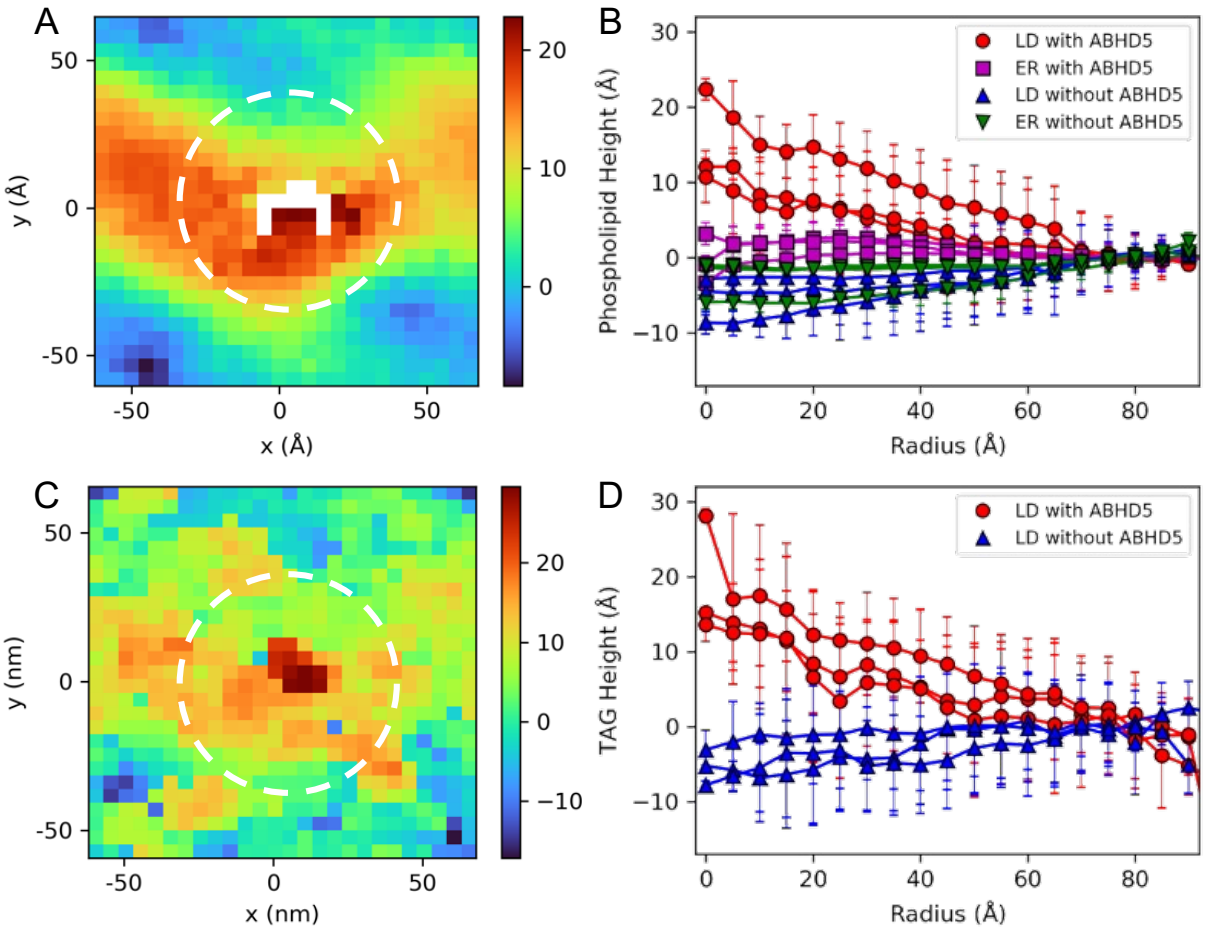
A
B
C
D
y (Å)
x (Å)
y (nm)
x (nm)
Phospholipid Height (Å)
TAG Height (Å)
Radius (Å)
LD with ABHD5
ER with ABHD5
LD without ABHD5
ER without ABHD5

Figure 7